

# Augmenting Implicit Neural Shape Representations with Explicit Deformation Fields

Matan Atzmon<sup>\* 1</sup>, David Novotny<sup>2</sup>, Andrea Vedaldi<sup>2</sup>, and Yaron Lipman<sup>1,2</sup>

<sup>1</sup>Weizmann Institute of Science, <sup>2</sup>Facebook AI Research

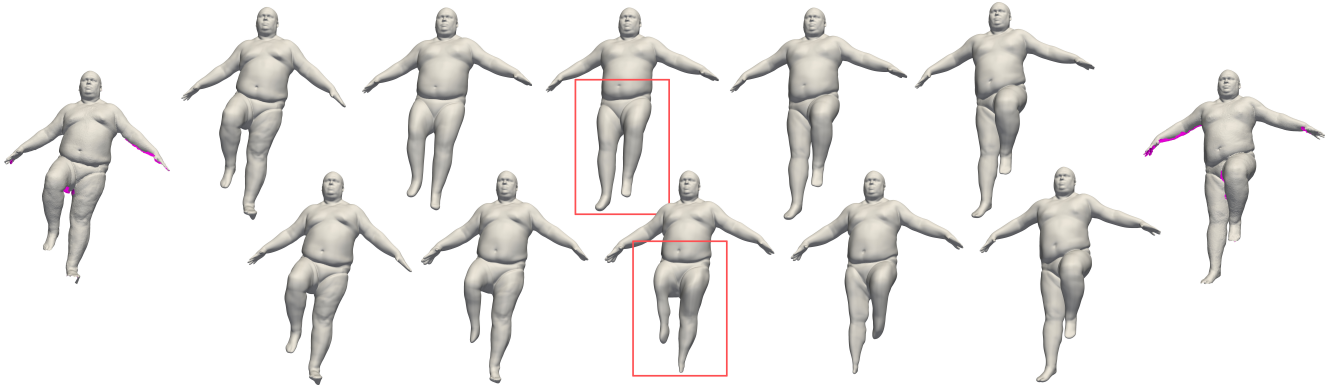


Figure 1: Augmenting implicit neural representations with consistent deformation fields allows incorporating deformation priors, *e.g.*, piecewise rigid, to shape space interpolations (top row); bottom row depicts state of the art implicit neural interpolation baseline; far left and right depict input raw scans.

## Abstract

*Implicit neural representation is a recent approach to learn shape collections as zero level-sets of neural networks, where each shape is represented by a latent code. So far, the focus has been shape reconstruction, while shape generalization was mostly left to generic encoder-decoder or auto-decoder regularization. In this paper we advocate deformation-aware regularization for implicit neural representations, aiming at producing plausible deformations as latent code changes. The challenge is that implicit representations do not capture correspondences between different shapes, which makes it difficult to represent and regularize their deformations. Thus, we propose to pair the implicit representation of the shapes with an explicit, piecewise linear deformation field, learned as an auxiliary function. We demonstrate that, by regularizing these deformation fields, we can encourage the implicit neural representation to induce natural deformations in the learned shape space, such as as-rigid-as-possible deformations.*

## 1. Introduction

The focal point of this work are implicit surfaces, defined as zero level-sets of scalar functions  $f : \mathbb{R}^3 \rightarrow \mathbb{R}$ ,

$$\mathcal{S} = \{x \in \mathbb{R}^3 \mid f(x) = 0\}.$$

The main benefit of an implicit shape representation is its ability to capture detailed continuous surfaces with arbitrary topology without requiring discretization, complex data structures, or explicit sampling.

Implicit surfaces recently found good pairing with neural networks. Representing an implicit function such as  $f$  with a neural network allows to leverage its expressive power to model accurately complex 3D scenes and objects [10, 3, 26, 35]. Neural implicit surfaces can also represent collections of 3D objects with different but related shapes. This is typically operationalized by conditioning the implicit function  $f$  with a latent code  $z \in \mathbb{R}^D$ :

$$\mathcal{S}(z) = \{x \in \mathbb{R}^3 \mid f(x, z) = 0\}.$$

By varying  $z$ , we can adjust the function’s zero level-set to match different members of the shape set. Indeed, recent

<sup>\*</sup>Work partially done during an internship at Facebook AI Research.

works [28, 25, 31] have demonstrated that, in this manner, it is possible to encode collections of complex 3D shapes of humans or human-made objects by low-dimensional latent code vectors.

Previous works have focused on the problem of obtaining high-fidelity reconstructions of a given set of 3D shapes from noisy or incomplete measurements such as point clouds or triangle soups. However, they have usually paid less attention to the shapes  $\mathcal{S}(z)$  generated by intermediate latent vectors  $z$ . For example, given that  $\mathcal{S}(z_1)$  and  $\mathcal{S}(z_2)$  reconstruct two shapes from the input dataset, do  $\mathcal{S}((1-t)z_1 + tz_2)$ ,  $t \in (0, 1)$ , form plausible intermediate shapes as well? In this paper we answer this question, with an aim to not just reconstructing a given set of shapes from sparse observations, but also to generalize the given examples to obtain a full shape space.

Previous works on learning shape spaces have usually relied on generic latent-space regularizers such as VAE [25, 3] or Auto-Decoders (AD) [31] that mainly enforce smoothness of latent code transitions. However, in many cases smoothness alone is not sufficient to learn plausible shapes. For example, in Figure 1 the bottom row shows implicit surfaces generated by interpolating the latent code obtained from state of the art implicit neural shape representations, demonstrating typical defects such as parts popping in and out of existence rather than deforming in a plausible manner.

Our main contribution is a new shape space regularization framework that encourages implicit neural shape representations to generate plausible interpolations of the training shapes. Intuitively, we would like different shapes to be related by plausible deformations, such as the one arising from articulation of the underlying physical object. However, differently from explicit shape representations such as meshes, implicit shapes do not provide point correspondences between deformations, which makes it difficult to apply standard geometric regularizers.

In order to address this challenge, we start from a careful analysis of the way neural level sets deform as the latent code changes. Inspired by classic level-set tracking methods [39, 41], we parameterize the collection of (non-unique) explicit vector fields, called *deformation fields*, that are consistent with the level-set deformation for a particular latent code change. Then, among these deformation fields, we seek the one that minimizes a geometric loss, consequently enforcing a geometric prior on the implicit neural representation  $f$ . We use in particular the as-rigid-as-possible energy, also known as Killing energy [6, 37, 36, 14, 13], due to its ability to encourage natural elastic or piece-wise rigid shape deformations.

Although we opt for a specific geometric prior in this paper, an important advantage of our framework is its generality: it allows to incorporate any desirable deformation

prior, which is expressible via explicit deformation fields, on the implicit neural shape space representation.

Empirically, we show that our framework, applied on the *raw* D-Faust dataset [7], can learn a plausible shape space, considerably improving upon existing baselines (see *e.g.* Figure 1 top vs bottom row). The power of our method is that, given unstructured and sparse data such as a triangle soup, it simultaneously achieves high-quality surface reconstructions, similar to previous work utilizing implicit shape representations, while also learning a space of plausible shapes generalizing the training samples. We provide both quantitative and qualitative results in the experimental section.

## 2. Related Work

### 2.1. Shape representations

Since our work considers learning of a shape space, below we revise the most relevant 3D shape representations.

**Implicit representations.** Implicit shape representations define a 3D shape as a level-set of a scalar function on  $\mathbb{R}^3$  (equation 1). Several works [43, 48, 17, 11] have explored representing such functions with voxel grids, which are implicit functions evaluated at 3D grids. Implicit functions on a continuous domain have been explored later [31, 49, 3, 2, 9, 25]. Park et al. [31] trained deep networks to label each 3D point with its signed distance from the nearest surface point on the boundary of a shape producing a signed distance field (SDF). Disn [49] improved the architecture of [31]. Preceding the deep learning era, SDFs were successfully applied to represent scene geometries in [27]. Atzmon et al. [3] fitted signed distance fields to raw data via a sign agnostic similarity loss, and [2] proposed to improve SDF learning via a differentiable parametrization of samples from the neural level-set. Deep occupancy fields, a specific kind of neural SDFs which reduce the distance function only to its sign, have been proposed in [9, 25].

Several works model shapes as compositions of well-defined 3D primitives. Genova et al. [16, 15] learn structured deep representations whose main components are Gaussian-shaped occupancy functions. Compositions of more explicitly defined mesh primitives were introduced in [23]. [46, 29] who split the 3D domain into Voronoi primitives and express their occupancies to delineate the surface.

The aforementioned approaches mostly improve the expressiveness of the representations to better model shape details. As such, our contribution is complimentary, as we focus on regularizing an arbitrary neural level-set predictor in order to improve generalization to test data.

**Explicit surfaces.** Instead of defining a surface implicitly as a function’s level-set, others explored more explicit rep-

representations, such as meshes. Notable deep mesh predictors were introduced in [19, 44]. [20, 47] proposed a more general representation that maps points from a fixed topological space (a 2D square) to 3D euclidean space. Others [42, 34, 24] represent shapes as a union over multi-view back-projections of the visible part of its surface.

## 2.2. Shape interpolation

Shape interpolation studies the problem of non-rigidly deforming a source 3D shape such that it matches a target template. In principle, there are infinitely many possible displacement trajectories that “flow” one shape to the other, which calls for an efficient regularizer that selects the most natural solution.

**ARAP surface regularization.** Similar to others, our work exploits the seminal as-rigid-as-possible (ARAP) paradigm [38] that constrains deformations to be as isometric as possible. In the context of vector fields that displace implicit surfaces, ARAP can be operationalized with the Killing energy [6]. A flow field with minimal Killing energy is denoted as-Killing-as-possible vector field (KVF) [6]. Solomon et al. [37] applied such KVFs to regularize 2D image warps.

KVFs were further applied to implicit surface tracking, which identifies trajectories of points attached to a time-evolving surface. The as-killing-as-possible constraint aided a surface point tracker in [41]. Previously, [39] proposed to track points with constant normal. Similar to [39, 41], we tie level-set points to move consistently on the surface. We differ from these works by using KVFs to learn the implicit surfaces’ *shape and motion*, rather than just tracking points on a given sequence. This introduces several new challenges such as the requirement of an explicit parameterization of consistent vectors fields and efficient (closed form) solution for the KVF at sampled implicit surfaces.

**Correspondence flows.** Slavcheva et al. [36] find a KVF that matches implicit surfaces of a pair of 3D scans. Eisenberger et al. [14] interpolate shapes by constructing a volume-preserving flow and minimizing a reconstruction and ARAP energies. [13] improves [14] by introducing additional momentum conservation constraints. Among learning-based methods, Limp [12] trains a mesh deformation network given ground truth 3D correspondences. [21, 45] differ from Limp by minimizing the Chamfer distance which does not require correspondence annotations. Our method is also unsupervised and takes as input raw 3D scans. Furthermore, we are the first to jointly consider the shape interpolation in the context of implicit neural shape space learning.

## 3. Method

Given a collection of input geometries,  $\mathcal{X}^{(i)} \subset \mathbb{R}^3$ ,  $i \in [m] := \{1, 2, \dots, m\}$  (e.g. manifold meshes, raw point-clouds, or triangle soups), our goal is to learn a *shape space*. In our case, this means a neural network  $f : \mathbb{R}^3 \times \mathbb{R}^D \rightarrow \mathbb{R}$ , where each latent vector  $\mathbf{z} \in \mathbb{R}^D$  represents a shape given by the implicitly-defined surface

$$\mathcal{S}(\mathbf{z}) = \{\mathbf{x} \in \mathbb{R}^3 \mid f_\theta(\mathbf{x}, \mathbf{z}) = 0\}, \quad (1)$$

where  $\theta \in \mathbb{R}^p$  are the learnable network parameters; in the following we will drop the  $\theta$  subscript of  $f$  for brevity. Two important properties of the shape space are: (i) All input shapes are represented, *i.e.*, for all shapes  $\mathcal{S}(\mathbf{z}^{(i)}) \approx \mathcal{X}^{(i)}$  for some  $\mathbf{z}^{(i)} \in \mathbb{R}^D$ ; and (ii) other latent vectors  $\mathbf{z} \in \mathbb{R}^D$  correspond to *plausible* shape deformations. For example, a shape  $\mathcal{S}(t\mathbf{z}^{(i)} + (1-t)\mathbf{z}^{(j)})$  for  $t \in (0, 1)$  would correspond to a natural deformation between  $\mathcal{S}(\mathbf{z}^{(i)})$  and  $\mathcal{S}(\mathbf{z}^{(j)})$ .

The first requirement of the shape spaces (i) is enforced as in previous works (detailed later). The main focus of this work is (ii), *i.e.*, regularizing  $f$  so to enforce plausible shape deformations as latent vectors change; this is done using consistent deformation fields, described next.

### 3.1. Consistent deformation fields

Consider a smooth change in latent codes  $\mathbf{z}(t)$ ,  $t \in (-\epsilon, \epsilon)$ , where  $\mathbf{z}(0) = \mathbf{z}_0 \in \mathbb{R}^D$  is the position at time  $t = 0$ , and  $\dot{\mathbf{z}}(0) = \boldsymbol{\eta} \in \mathbb{R}^D$  is the speed at  $t = 0$ . Integrated, this process generates a curve in latent space describing a deformation of the shapes,  $\mathcal{S}(\mathbf{z}(t))$ . We would like to incorporate a prior on this deformation. For example, in many applications the shape deformations are expected to be locally approximately rigid (e.g., because the deformation is driven by an articulated skeleton).

The challenge of imposing such a rigidity constraint is that the shapes are given to us implicitly as zero level-sets of a neural network,  $f(\mathbf{x}, \mathbf{z}(t))$ . Differently from the case of meshes, where the trajectory of individual vertices is known, with implicit surfaces the motion of 3D points is only known up to a shift along the surface. We thus propose to supplement the implicit representation with explicit consistent vector fields  $\mathbf{v}$  of point displacements that provide all possible explanations of the deformation of the surface  $\mathcal{S}(\mathbf{z}(t))$ , and use the latter to define deformation priors. Consistent vector fields have been previously considered for tracking known/input sequences of implicit surfaces [39, 41]. Here, we use them to facilitate the learning of a space of deformable implicit surfaces.

We call a vector field  $\mathbf{v} = \mathbf{v}_{\mathbf{z}_0, \boldsymbol{\eta}} : \mathbb{R}^3 \rightarrow \mathbb{R}^3$  *consistent* with the latent motion  $\mathbf{z}(t)$  if, for all  $\mathbf{x} \in \mathcal{S}(\mathbf{z}_0)$ , it satisfies the constraint

$$\left. \frac{d}{dt} \right|_{t=0} f(\mathbf{x} + t\mathbf{v}(\mathbf{x}), \mathbf{z}(t)) = 0. \quad (2)$$

Intuitively, this means that, given a point  $x$  that belongs to the implicit surface at time 0, *i.e.*,  $x \in \mathcal{S}(z_0)$ , then moving  $x$  at speed  $v(x)$  will keep the point on the surface  $\mathcal{S}(z(t))$  for small (infinitesimal) times  $t$ . The chain rule allows writing eq. (2) more explicitly as

$$\nabla_x f v + \frac{\partial f}{\partial z} \eta = 0, \quad (3)$$

where  $f$  is evaluated at  $(x, z_0)$ , and  $\nabla_x f \in \mathbb{R}^{1 \times 3}$  denotes the gradient of  $f$ . Equation (3) is an under-determined linear system in  $v \in \mathbb{R}^3$  and its general solution can be written as a sum of a particular solution and the kernel of  $\nabla_x f(x, z_0)$ . Specifically, we write  $v = w + w^\perp$  where  $w = w_{z_0, \eta}$  is the particular solution to eq. (3) given by

$$w = -\frac{\nabla_x f^T \frac{\partial f}{\partial z} \eta}{\|\nabla_x f\|^2} \eta, \quad (4)$$

and  $w^\perp$  is any vector perpendicular to  $\nabla_x f(x, z_0)$ . We let  $w^\perp = Pu$ , where  $u : \mathbb{R}^3 \rightarrow \mathbb{R}^3$  is an arbitrary vector field, and  $P$  is the projection matrix on  $\nabla_x f^\perp$  (*i.e.*, the tangent space to  $\mathcal{S}(z_0)$  at  $x$ ) defined by

$$P = I - \frac{\nabla_x f^T \nabla_x f}{\|\nabla_x f\|^2}, \quad (5)$$

where  $I \in \mathbb{R}^{3 \times 3}$  is the identity matrix. In this manner, we can write the space of consistent vector fields, *i.e.* the fields

$$v = v_{z_0, \eta, u} : \mathcal{S}(z_0) \rightarrow \mathbb{R}^3$$

that satisfy eq. (3), as

$$v = w + Pu. \quad (6)$$

Intuitively, eq. (6) represents the space of possible motions of the surface points that are consistent with the implicit shape deformation, where the ambiguity here comes from the fact that a point  $x$  can also move arbitrarily in the tangent directions to the surface  $\mathcal{S}(z_0)$  without compromising consistency.

### 3.2. Deformation priors

Now that consistent vector fields  $v$  are introduced, we are ready to impose deformation priors on the shape space. The deformation priors will take the form

$$\text{loss}_d(\theta) = \min_u \mathbb{E}_{z, \eta, x} \rho(x; v_{z, \eta, u}), \quad (7)$$

where the latent code  $z$  and variation  $\eta$  are sampled according to some distribution  $\mathcal{D} = \mathcal{D}(\mathbb{R}^D \times \mathbb{R}^D)$ , the 3D point

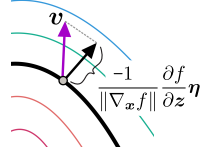


Figure 2: Consistent deformation field.

$x$  is sampled from some distribution over the corresponding surface  $\mathcal{S}(z)$ , and  $\rho(x; v)$  is a measure of deformation induced by the field  $v$  at location  $x$ . As commonly done, we approximate the expectation in eq. (7) with the empirical expectation

$$\text{loss}_d(\theta) = \min_u \frac{1}{n} \sum_{i=1}^n \rho(x_i; v_{z_i, \eta_i, u}), \quad (8)$$

where we consider  $n$  samples,  $(z_i, \eta_i) \sim \mathcal{D}$  and  $x_i \in \mathcal{S}(z_i)$ ,  $i \in [n]$ . Since all choices of  $u$  correspond to consistent deformation fields, taking the minimum w.r.t.  $u$  is important to ensure we are considering the deformation field with lowest deformation error explaining the current shape space deformation  $z(t)$ . In the following example, we demonstrate why taking an arbitrary consistent vector field instead of the optimal one is insufficient.

**Example.** We provide a simple example of a rigid movement of an implicit shape with a non rigid consistent deformation field. Consider the implicit function

$$f(x, t) = \|x - t\eta\|^2 - 1,$$

representing a unit sphere translated with constant velocity  $\eta$ . The consistency eq. (3) evaluated at  $t = 0$  in this case is

$$\langle x, v - \eta \rangle = 0$$

for all  $x \in \mathcal{S}(0)$ , *i.e.*,  $\|x\| = 1$ . Therefore  $w = \frac{\langle x, \eta \rangle}{\|\eta\|^2} x$  is a particular solution to the consistency equation, see fig. 3 (in green). Now consider the two points on the sphere  $x_1 = \frac{\eta}{\|\eta\|}$  and  $x_2 = \frac{\eta^\perp}{\|\eta\|}$ , where  $\eta^\perp$  is an orthogonal vector to  $\eta$ , so that  $w(x_1) = \eta$  while  $w(x_2) = 0$ . Thus, while the surface is moving rigidly with uniform velocity  $\eta$ , we have found an “alternative” velocity field  $w$  that is compatible with the change in the implicit function, but that causes the distance between the surface points  $x_1$  and  $x_2$  to change. We can recover the “true” velocity field by setting the auxiliary vector  $u(x_i) = \eta$ , which results in  $v(x_i) = w(x_i) + Pu(x_i) = \eta$  for  $i = 1, 2$ .

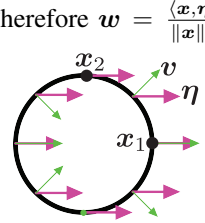


Figure 3: Non-rigid consistent field  $v$ .

**Killing energy.** The Killing energy [37, 41, 36] is applied to vector fields and measures their deviation from vector fields induced from rigid motions, making it an obvious choice of regularizer in our case. The Killing energy of a vector field  $v$  is defined as

$$\rho(x; v) = \|\nabla_x v(x) + \nabla_x v(x)^T\|_F^2. \quad (9)$$



**Rigid deformation prior.** Next, we look at the problem of predicting the auxiliary vector field  $\mathbf{u}(\mathbf{x})$ . For this, we may use a sophisticated regressor such as a second neural network, but this is prone to overfitting. From the example above,  $\mathbf{u}$  should approximate the velocity field of the object, which is locally rigid. If the motion was globally rigid (*i.e.*,  $\mathbf{x}(t) = R_t \mathbf{x}(0) + T_t$  for time-varying  $(R_t, T_t) \in SE(3)$ ), then it could be explained by an affine choice of velocity field:

$$\mathbf{u}(\mathbf{x}) = \mathbf{A}\mathbf{x} + \mathbf{b}, \quad (10)$$

where  $(\mathbf{A}, \mathbf{b}) \in \mathbb{R}^{3 \times 4}$  (this can be seen by differentiating  $\mathbf{x}(t)$  with respect to time). Now plugging eq. (10) in eq. (6) and taking the derivative w.r.t.  $\mathbf{x}$  gives:

$$\nabla_{\mathbf{x}} \mathbf{v} = \nabla_{\mathbf{x}} \mathbf{w} + (D_{\mathbf{x}} \mathbf{P})(\mathbf{A}\mathbf{x} + \mathbf{b}) + \mathbf{P}\mathbf{A},$$

where, for a vector  $\mathbf{q} = (q_1, q_2, q_3)^T$ , we denote  $[(D_{\mathbf{x}} \mathbf{P})\mathbf{q}]_i = \sum_{j=1}^3 \nabla_{\mathbf{x}} P_{ij}(\mathbf{x}) q_j$ . Using this in eqs. (8) and (9) leads to a least-squares (LS) problem in  $\mathbf{A}, \mathbf{b}$ . Minimization w.r.t.  $\mathbf{A}, \mathbf{b}$  is done by solving the normal equations. Let  $\mathbf{A}_*, \mathbf{b}_*$  denote the minimizer of this LS problem, so that  $\mathbf{u}_*(\mathbf{x}) = \mathbf{A}_* \mathbf{x} + \mathbf{b}_*$ . Plugging  $\mathbf{u}_*$  in eq. (8) yields

$$\text{loss}_d(\theta) = \frac{1}{n} \sum_{i=1}^n \rho(\mathbf{x}_i; \mathbf{v}_{\mathbf{z}_i, \boldsymbol{\eta}_i, \mathbf{u}_*}). \quad (11)$$

Clearly, the two losses in equations eq. (11) and eq. (8) share the same value at  $\theta$ . Furthermore, Danskin's Theorem (see supplementary) asserts that they also have the same gradient at  $\theta$ .

**Multiple rigid deformation priors.** A single affine  $\mathbf{u}$  can explain a global rigid motion of the implicit shape. Combining a collection of such affine fields can be used to introduce a piecewise rigid motion prior. In order to do so, we introduce probability vector, also modeled with a neural network (we will continue to denote the collection of all learnable parameters by  $\theta$ ),  $\mathbf{p} = (p_1, \dots, p_k) : \mathbb{R}^3 \rightarrow [0, 1]^k$ , where  $k$  is a hyper-parameter and  $\sum_{j=1}^k p_j(\mathbf{x}) = 1$  for all  $\mathbf{x}$ . We then introduce  $k$  affine fields  $\mathbf{u}_j(\mathbf{x}) = \mathbf{A}_j \mathbf{x} + \mathbf{b}_j$ ,  $j \in [k]$ , and define our deformation loss as:

$$\text{loss}_d(\theta) = \min_{\mathbf{u}_1, \dots, \mathbf{u}_k} \frac{1}{n} \sum_{j=1}^k \sum_{i=1}^n p_j(\mathbf{x}_i) \rho(\mathbf{x}_i; \mathbf{v}_{\mathbf{z}_i, \boldsymbol{\eta}_i, \mathbf{u}_j}) \quad (12)$$

This loss divides the surface  $\mathcal{S}(\mathbf{x})$  to (soft) pieces according to the probability vector  $\mathbf{p}$ , and encourages each piece to be deformed with a rigid motion. Minimization w.r.t.  $\mathbf{u}_1, \dots, \mathbf{u}_k$  can be done independently for each  $j \in [k]$ , as in the case of a single rigid deformation prior. The only difference is the incorporation of weights  $p_j(\mathbf{x}_i)$ , leading to a weighted LS problem. Using Danskin's theorem again will guarantee that plugging the minimizing fields  $\mathbf{A}_j^*, \mathbf{b}_j^*$  in the loss in eq. (12) provides correct value and gradient at current parameter  $\theta$ .

## 4. Implementation details

In addition to the deformation prior  $\text{loss}_d$ , which is the main contribution of this work and described in the previous section, we use standard reconstruction losses for the shape space requirement (i), *i.e.*,  $\mathcal{S}(\mathbf{z}^{(i)}) \approx \mathcal{X}^{(i)}$ ,  $i \in [m]$ . In this section we provide the remaining details on our loss and architecture.

We use two networks in our system, the implicit representation  $f : \mathbb{R}^3 \times \mathbb{R}^D \rightarrow \mathbb{R}$ , and the probability network  $\mathbf{p} = (p_1, \dots, p_k) : \mathbb{R}^3 \times \mathbb{R}^D \rightarrow \mathbb{R}^k$ . We use  $k = 20$  unless otherwise stated, an ablation test on  $k$  is provided in the supplementary. Both networks are Multilayer Perceptrons (MLPs) (specific architectures are in the supplementary).  $\mathbf{p}(\mathbf{x}, \mathbf{z})$  represents the parts' probabilities of a point  $\mathbf{x}$  in the shape  $\mathcal{S}(\mathbf{z})$ . We use the Auto-Decoder (AD) paradigm [31], where the latent codes  $\mathcal{Z} = \{\mathbf{z}^{(i)}\}_{i \in [m]}$  are learnable parameters. We incorporate the AD regularizer encouraging the latent codes to have a scaled Gaussian distribution (see [31] for more details),

$$\text{loss}_{\text{ad}}(\theta) = \frac{1}{m} \sum_{i=1}^m \|\mathbf{z}^{(i)}\|^2, \quad (13)$$

where  $\|\mathbf{z}\| = \sqrt{\mathbf{z}^T \mathbf{z}}$  is the standard euclidean norm, and we henceforth denote by  $\theta$  the collection of all learnable parameters of the system, including the parameters of  $f, \mathbf{p}$ , and  $\mathcal{Z}$ .

**Deformation loss.** We use eq. (12) as our deformation loss, where the samples  $\mathbf{z}_i, \boldsymbol{\eta}_i, \mathbf{x}_i$  used for each iteration are constructed as follows. For each  $i \in [n]$  in a batch of size  $n$ , we random a pair of latent codes  $\mathbf{z}^{(i_1)}, \mathbf{z}^{(i_2)}$  from  $\mathcal{Z}$ , and a scalar  $t$  uniformly in  $[0, 1]$ . Next, we define  $\mathbf{z}_i$  to be the time  $t$  interpolation of  $\mathbf{z}^{(i_1)}$  and  $\mathbf{z}^{(i_2)}$ . We have tested two options: *linear*, where  $\mathbf{z}_i = (1 - t)\mathbf{z}^{(i_1)} + t\mathbf{z}^{(i_2)}$ , and *spiral*, where

$$\mathbf{z}_i = \left[ (1 - t)\|\mathbf{z}^{(i_1)}\| + t\|\mathbf{z}^{(i_2)}\| \right] \text{slerp} \left( \frac{\mathbf{z}^{(i_1)}}{\|\mathbf{z}^{(i_1)}\|}, \frac{\mathbf{z}^{(i_2)}}{\|\mathbf{z}^{(i_2)}\|} \right)$$

and *slerp* is spherical linear interpolation. We found the spiral interpolation favorable since it does not decrease the interpolated latent codes norm; we compare between the two options in the experimental section. For each such  $\mathbf{z}_i$ , we set  $\boldsymbol{\eta}_i$  to be the normalized speed  $\frac{d\mathbf{z}_i}{dt}$  of the interpolation, and  $\mathbf{x}_i$  a random sample from  $\mathcal{S}(\mathbf{z}_i)$  computed by projecting a random point in space onto  $\mathcal{S}(\mathbf{z}_i)$  as detailed in the supplementary. We also add the Eikonal loss [18], denoted  $\text{loss}_e$ , to regularize the level-sets of implicit surfaces at intermediate latent codes  $\mathbf{z}_i$ , see supplementary for details.

**Reconstruction loss.** In order to approximate the input shapes  $\mathcal{X}^{(i)}$  at the latent codes  $\mathbf{z}^{(i)}$ , we use the SALD reconstruction loss [4], denoted  $\text{loss}_r$ , that handles raw data as

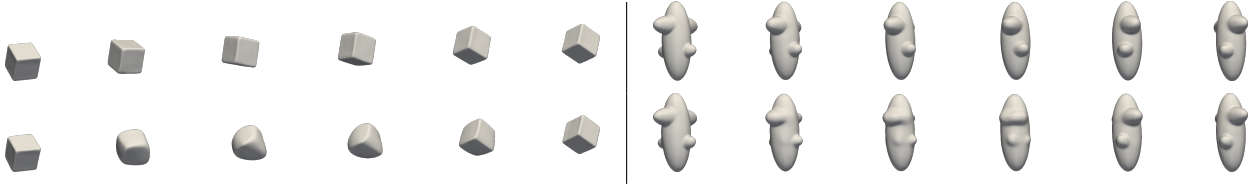


Figure 4: Toy dataset: incorporating the deformation prior loss<sub>d</sub> (top row) allows reconstructing natural shape interpolation, in contrast to baseline (bottom row). Left and right in each sequence are the reconstructed input shapes.

input, and only requires the *unsigned* distance to the input geometry,  $d(\mathbf{x}, \mathcal{X}) = \min_{\mathbf{y} \in \mathcal{X}} \|\mathbf{x} - \mathbf{y}\|$ . See supplementary for details on this loss. Our complete loss function is

$$\text{loss} = \text{loss}_r + \lambda_d \text{loss}_d + \lambda_e \text{loss}_e + \lambda_{ad} \text{loss}_{ad}, \quad (14)$$

where the losses are all functions of the parameters  $\theta$ , and we use  $\lambda_e = 0.1$ , and  $\lambda_{ad} = 0.001$ . For  $\lambda_d$  we use scheduling, details in the supplementary.

## 5. Experiments

**Baselines.** For baselines we picked two popular implicit shape space learning methods that have been shown to produce state of the art results on the same or similar datasets: (i) Auto-Decoder (AD) [31]; and (ii) Variational Auto-Encoder (VAE) [25]. In both cases, we trained using the SALD reconstruction loss [4]. For the encoder in the VAE, we use PointNet [33], similar to previous works that utilizing VAE on this task [25, 3, 4]. The full details of the network architecture can be found in supplementary.

### 5.1. Evaluation using toy data

In the first experiment, we test the ability of our model to learn from a synthetic shape space with known and well understood deformations between shapes. To this end, we generated two “toy” datasets: (i) 12 cubes, randomly rotated and translated in 3D space; and (ii) 12 ellipsoids (“main body”) with upper and bottom perturbing part (“arms” and “legs”), where the main body ellipsoid is randomly translated in the  $x$ -axis direction and the arms and legs ellipsoids are deformed by two different random rotations around the  $z$ -axis. For each pair of shapes in this dataset there exists a two-piece rigid deformation field, deforming one shape to the other. See the supplementary for a video showing few samples of shapes from the two datasets.

On each of these datasets we trained: (i) Vanilla auto-decoder, *i.e.*, without our deformation prior loss,  $\lambda_d = 0$ ; and (ii) using the same auto-decoder architecture and loss as in (i), but now with active deformation loss, *i.e.*,  $\lambda_d = 0.001$ . We set  $k$  to 1 for the cubes and 2 for the ellipses to match the ground truth number of parts.

The bottom and upper row in fig. 4 show learned implicit shapes for  $\lambda_d = 0$  and  $\lambda_d = 0.001$ , respectively. In each sequence, the leftmost and rightmost shapes correspond to a

	Method	Registrations		Scans	
		Chamfer	Wasserstein	Chamfer	Wasserstein
Unique action	Ours	<b>0.112</b>	<b>2.994</b>	<b>0.098</b>	<b>2.971</b>
	AD	0.231	3.527	0.195	3.354
	VAE	0.237	3.361	0.146	3.226
Punching	Ours	<b>0.126</b>	<b>3.164</b>	<b>0.103</b>	<b>3.069</b>
	AD	0.995	3.757	0.198	3.671
	VAE	0.656	4.558	0.613	4.351
One leg jump	Ours	<b>0.278</b>	<b>3.490</b>	<b>1.313</b>	<b>5.601</b>
	AD	0.385	3.961	1.414	5.908
	VAE	0.957	5.077	1.992	7.064
Light hopping	Ours	0.053	<b>2.801</b>	0.045	2.871
	AD	<b>0.050</b>	2.818	<b>0.041</b>	<b>2.857</b>
	VAE	0.086	2.906	0.081	2.903
Shake hips	Ours	<b>0.097</b>	<b>3.016</b>	<b>0.211</b>	<b>3.358</b>
	AD	0.128	3.228	0.244	3.532
	VAE	0.217	3.258	0.343	3.469

Table 1: Reconstruction of test set of all humans (splits 1 and 2) in D-Faust. We log Chamfer and Wasserstein distances of the reconstructed surfaces to the raw scans and ground-truth registrations; Chamfer reported  $\times 10^3$ .

pair of learned latent codes  $\mathbf{z}^{(i_1)}, \mathbf{z}^{(i_2)}$ ,  $i_1, i_2 \in [12]$ . Note that both methods learn to reconstruct the input data well. The middle shapes in this experiment were generated using linear interpolation of latent codes,  $(1-t)\mathbf{z}^{(i_1)} + t\mathbf{z}^{(i_2)}$ ,  $t \in [0.15, 0.35, 0.65, 0.85]$ . Note, in particular, that the shapes generated with  $\lambda_d = 0$  fail to keep important geometrical features and revert to smooth but “non-geometrical” interpolation. This can be seen from the smoothing of the cubes and the blending of the arms and legs in the ellipsoid. In contrast, enabling the deformation loss leads to geometrically-plausible interpolations, close to the ground-truth ones.

### 5.2. Shape space learning

Next, we test our deformation prior on the task of learning a shape space from “real-life” raw scans. We considered the D-Faust raw scans dataset [8], consisting of 41k scans from 10 humans: 5 male and 5 female. The data for each individual is categorized into sequences of actions. Together with the raw data, mesh registrations are also in the dataset. We use the registrations for evaluation, but not for training.

**Shape space reconstruction.** To test the ability of our learned shape space to generalize and represent unseen geometries from sparse training examples, we have created the following data splits from the D-Faust dataset: (1) *Unique*

	Method	Registrations		Scans	
		Chamfer	Wasserstein	Chamfer	Wasserstein
Male random	Ours (spiral)	0.073	<b>3.329</b>	0.048	<b>3.233</b>
	Ours (linear)	0.080	3.360	0.051	3.328
	AD	<b>0.071</b>	3.361	<b>0.045</b>	3.292
	VAE	0.128	3.503	0.164	3.457
Female random	Ours (spiral)	0.042	2.490	0.042	2.530
	Ours (linear)	<b>0.036</b>	<b>2.450</b>	<b>0.036</b>	<b>2.470</b>
	AD	0.056	2.600	0.049	2.640
	VAE	0.163	2.841	0.152	2.842
Male action	Ours (spiral)	1.017	6.410	0.822	5.360
	Ours (linear)	<b>0.762</b>	<b>5.499</b>	<b>0.649</b>	<b>4.616</b>
	AD	1.201	6.657	0.979	5.613
	VAE	2.443	9.171	2.270	8.182
Female action	Ours (spiral)	<b>0.048</b>	<b>2.518</b>	<b>0.042</b>	<b>2.456</b>
	Ours (linear)	0.052	2.633	0.045	2.620
	AD	0.068	2.806	0.059	2.709
	VAE	8.509	17.024	8.547	16.951

Table 2: Reconstruction of test set of individuals (splits 3 and 4) in D-Faust. We log the Chamfer and Wasserstein distances of the reconstructed surfaces to the raw scans and ground-truth registrations; Chamfer reported  $\times 10^3$ .

*action*: removes a unique action from each of the 10 human identities as a test set, and trains on every 5-th scan from the remaining time-ordered scans; (2) *Punching/One leg jump/Light hopping/Shake hips*: removes the same action from all 10 humans as a test set, and trains on every 5th scan of the time-ordered remainder. (3) *Male action/Female action*: takes one action from each human as a test set, and out of a tuple  $\mathcal{F}$  of all remaining ordered frames takes every 10-th for training. (4) *Male random/Female random*: uses the same training set as (3), but from every 10 consecutive frames in  $\mathcal{F}$ , randomly samples from frames 1-9 for testing. In general, since all these data splits are still very large, we randomly subsampled 5%-10% of the scans for experimentation.

To test how well the learned shape space represents unseen test cases, we follow [31] and, for each test scan  $\mathcal{X}$ , we minimize the reconstruction loss with respect to the latent code  $z \in \mathbb{R}^D$  with the weights of the neural network  $f$  fixed. Table 1 and table 2 report the results on splits 1 and 2 (all humans), and on splits 3 and 4 (individuals) respectively. In the latter, we also provide a comparison between linear and spiral interpolations. Figure 6 shows some typical results from splits 1 and 2; we show failure cases in the supplementary. In order to measure reconstruction accuracy we use the Chamfer and Wasserstein distances, as customary (details in the supplementary). As can be seen by inspecting the quantitative and qualitative results, our deformation prior indeed improves prediction ability to unseen scans representing a missing action or pose. For example, when comparing the red boxes in Figure 6 to the blue boxes (unseen ground truth) our method is able to reconstruct the most similar pose, outperforming the baselines. Figure 5 depicts the probability vectors (a different color for each of

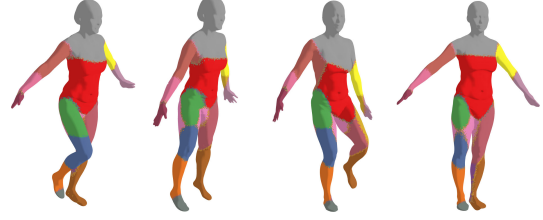


Figure 5: The learned probabilities  $p$  for several reconstructions from the female split (splits 3 and 4).

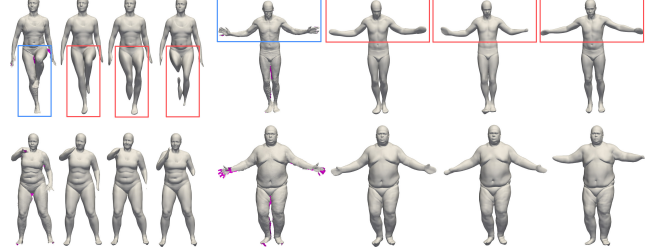


Figure 6: Shape space reconstruction of unseen poses (taken from splits 1,2 and 4). From left to right (in each sequence of 4): unseen raw scan, ours, AD, VAE.

	Method	HKS( $t_{\min}$ )	HKS( $t_{\text{mean}}$ )	HKS( $t_{\max}$ )	area	geodesic
Male	Ours (slerp)	955.422	<b>4.804</b>	<b>4.775</b>	<b>120.632</b>	<b>0.717</b>
	Ours (linear)	<b>775.381</b>	4.946	4.914	179.856	0.977
	AD	1004.734	6.150	6.104	189.676	1.119
Female	Ours (slerp)	<b>191.823</b>	<b>6.511</b>	<b>6.433</b>	<b>106.807</b>	<b>0.836</b>
	Ours (linear)	239.745	7.664	7.584	143.439	1.073
	AD	468.887	14.830	14.669	151.859	1.203

Table 3: Evaluation of interpolated surfaces. Wasserstein distance between histograms of different surface properties; HKS numbers are  $\times 10^6$ ; area and geodesic  $\times 10^3$ .

the  $k = 20$  pieces) for reconstructed examples of the Female (splits 3 and 4). Interestingly, the vectors correspond to the natural kinematic structure of the body.

### 5.3. Shape space interpolation

We evaluated shape space interpolations on the individual splits (splits 3 and 4). The interpolations are using the spiral interpolation of learned latent codes  $\mathcal{Z}$ . Figure 7 presents qualitative results; note that our deformation prior improves intermediate poses and alleviates shortening of limbs that are common with the baselines. For example, note that the highlighted face, hand, and legs in the red boxes are either distorted or deformed in the baselines compared to the interpolation end points (blue boxes), while our method maintains the geometric properties of these parts. For qualitative assessment of the interpolation results, we have compared histograms of different surface properties such as Heat Kernel Signature (HKS) at times  $t_{\min}$ ,  $t_{\text{mean}} = 0.5(t_{\min} + t_{\max})$ , and  $t_{\max}$  as suggested in [40],

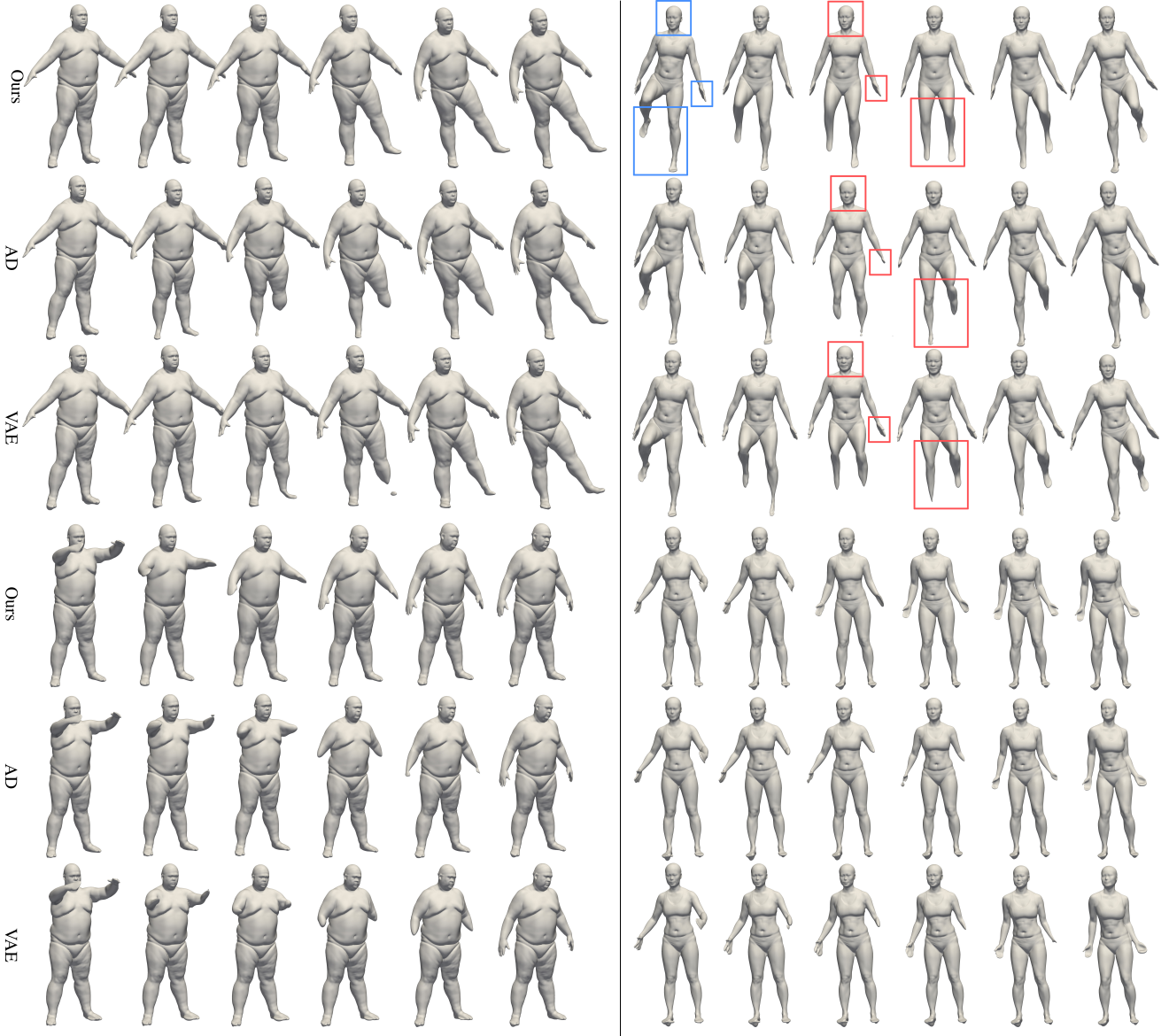


Figure 7: Interpolation of latent codes. Each block of three rows shows (top to bottom): Our result, AD, and VAE. Note the natural shape and motion of the intermediate shapes when incorporating our deformation prior.

surface area, and pairwise geodesic distances [30]. In Table 3 we log the Wasserstein distances between histograms of interpolated surfaces and the corresponding histograms of the reconstructed shapes generated the interpolation (*i.e.*, far left and right in each sequence in Figure 7). Note the advantage in using spiral interpolation method.

## 6. Conclusions

In this paper we have analyzed the ability of deep neural implicit surfaces to interpolate between members of a set of complex 3D shapes, such as articulated human bodies.

To this end, we proposed a novel framework that regularizes the deformations within an implicit neural shape space. The latter is done by first expressing the 3D deformation fields generated by an infinitesimal change of a latent shape code, followed by regularizing these fields to be a collection of approximately rigid motions with an as-rigid-as-possible regularizer. The experimental section has demonstrated that our framework significantly improves the generalization of the state of the art implicit shape representation networks especially when trained on a sparse and temporally non-smooth collection of 3D shapes, such as a heavily subsampled version of the raw D-Faust dataset.

## References

- [1] Panos Achlioptas, Olga Diamanti, Ioannis Mitliagkas, and Leonidas Guibas. Learning representations and generative models for 3d point clouds. In *International conference on machine learning*, pages 40–49. PMLR, 2018.
- [2] Matan Atzmon, Niv Haim, Lior Yariv, Ofer Israelov, Haggai Maron, and Yaron Lipman. Controlling neural level sets. In *Advances in Neural Information Processing Systems*, pages 2032–2041, 2019.
- [3] Matan Atzmon and Yaron Lipman. Sal: Sign agnostic learning of shapes from raw data. In *IEEE/CVF Conference on Computer Vision and Pattern Recognition (CVPR)*, June 2020.
- [4] Matan Atzmon and Yaron Lipman. Sald: Sign agnostic learning with derivatives. *arXiv preprint arXiv:2006.05400*, 2020.
- [5] Tamer Başar and Pierre Bernhard. *H-infinity optimal control and related minimax design problems: a dynamic game approach*. Springer Science & Business Media, 2008.
- [6] Mirela Ben-Chen, Adrian Butscher, Justin Solomon, and Leonidas Guibas. On discrete killing vector fields and patterns on surfaces. In *Computer Graphics Forum*, volume 29, pages 1701–1711. Wiley Online Library, 2010.
- [7] Federica Bogo, Javier Romero, Gerard Pons-Moll, and Michael J. Black. Dynamic FAUST: Registering human bodies in motion. In *IEEE Conf. on Computer Vision and Pattern Recognition (CVPR)*, July 2017.
- [8] Federica Bogo, Javier Romero, Gerard Pons-Moll, and Michael J. Black. Dynamic FAUST: registering human bodies in motion. In *Proc. CVPR*, 2017.
- [9] Zhiqin Chen and Hao Zhang. Learning implicit fields for generative shape modeling. In *Proceedings of the IEEE Conference on Computer Vision and Pattern Recognition*, pages 5939–5948, 2019.
- [10] Julian Chibane, Gerard Pons-Moll, et al. Neural unsigned distance fields for implicit function learning. *Advances in Neural Information Processing Systems*, 33, 2020.
- [11] Christopher B Choy, Danfei Xu, JunYoung Gwak, Kevin Chen, and Silvio Savarese. 3d-r2n2: A unified approach for single and multi-view 3d object reconstruction. In *European conference on computer vision*, pages 628–644. Springer, 2016.
- [12] Luca Cosmo, Antonio Norelli, Oshri Halimi, Ron Kimmel, and Emanuele Rodolà. Limp: Learning latent shape representations with metric preservation priors. In *Computer Vision - ECCV 2020 - 16th European Conference, Glasgow, UK, August 23-28, 2020, Proceedings, Part III*, volume 12348, pages 19–35. Springer, 2020.
- [13] Marvin Eisenberger and Daniel Cremers. Hamiltonian dynamics for real-world shape interpolation. In *Computer Vision - ECCV 2020 - 16th European Conference, Glasgow, UK, August 23-28, 2020, Proceedings, Part IV*, volume 12349, pages 179–196. Springer, 2020.
- [14] Marvin Eisenberger, Zorah Löhner, and Daniel Cremers. Divergence-free shape correspondence by deformation. In *Computer Graphics Forum*, volume 38, pages 1–12. Wiley Online Library, 2019.
- [15] Kyle Genova, Forrester Cole, Avneesh Sud, Aaron Sarna, and Thomas Funkhouser. Local deep implicit functions for 3d shape. In *Proceedings of the IEEE/CVF Conference on Computer Vision and Pattern Recognition*, pages 4857–4866, 2020.
- [16] Kyle Genova, Forrester Cole, Daniel Vlasic, Aaron Sarna, William T Freeman, and Thomas Funkhouser. Learning shape templates with structured implicit functions. In *Proceedings of the IEEE International Conference on Computer Vision*, pages 7154–7164, 2019.
- [17] Rohit Girdhar, David F Fouhey, Mikel Rodriguez, and Abhinav Gupta. Learning a predictable and generative vector representation for objects. In *European Conference on Computer Vision*, pages 484–499. Springer, 2016.
- [18] Amos Gropp, Lior Yariv, Niv Haim, Matan Atzmon, and Yaron Lipman. Implicit geometric regularization for learning shapes. In *Proceedings of Machine Learning and Systems 2020*, 2020.
- [19] Thibault Groueix, Matthew Fisher, Vladimir G Kim, Bryan C Russell, and Mathieu Aubry. 3d-coded: 3d correspondences by deep deformation. In *Proceedings of the European Conference on Computer Vision (ECCV)*, pages 230–246, 2018.
- [20] Thibault Groueix, Matthew Fisher, Vladimir G Kim, Bryan C Russell, and Mathieu Aubry. A papier-mâché approach to learning 3d surface generation. In *Proceedings of the IEEE conference on computer vision and pattern recognition*, pages 216–224, 2018.
- [21] Chiyu Jiang, Jingwei Huang, Andrea Tagliasacchi, Leonidas Guibas, et al. Shapeflow: Learnable deformations among 3d shapes. *arXiv preprint arXiv:2006.07982*, 2020.
- [22] Diederik P Kingma and Jimmy Ba. Adam: A method for stochastic optimization. *arXiv preprint arXiv:1412.6980*, 2014.
- [23] Lingxiao Li, Minhyuk Sung, Anastasia Dubrovina, Li Yi, and Leonidas J Guibas. Supervised fitting of geometric primitives to 3d point clouds. In *Proceedings of the IEEE Conference on Computer Vision and Pattern Recognition*, pages 2652–2660, 2019.
- [24] Zhaoliang Lun, Matheus Gadelha, Evangelos Kalogerakis, Subhransu Maji, and Rui Wang. 3d shape reconstruction from sketches via multi-view convolutional networks. In *2017 International Conference on 3D Vision (3DV)*, pages 67–77. IEEE, 2017.
- [25] Lars Mescheder, Michael Oechsle, Michael Niemeyer, Sebastian Nowozin, and Andreas Geiger. Occupancy networks: Learning 3d reconstruction in function space. In *Proceedings of the IEEE Conference on Computer Vision and Pattern Recognition*, pages 4460–4470, 2019.
- [26] Ben Mildenhall, Pratul P. Srinivasan, Matthew Tancik, Jonathan T. Barron, Ravi Ramamoorthi, and Ren Ng. NeRF: Representing scenes as neural radiance fields for view synthesis. In *Proc. ECCV*, 2020.
- [27] Richard A Newcombe, Shahram Izadi, Otmar Hilliges, David Molyneaux, David Kim, Andrew J Davison, Pushmeet Kohi, Jamie Shotton, Steve Hodges, and Andrew Fitzgibbon. Kinectfusion: Real-time dense surface mapping and track-



- ing. In *2011 10th IEEE International Symposium on Mixed and Augmented Reality*, pages 127–136. IEEE, 2011.
- [28] Michael Niemeyer, Lars M. Mescheder, Michael Oechsle, and Andreas Geiger. Occupancy flow: 4d reconstruction by learning particle dynamics. In *Proc. ICCV*, 2019.
  - [29] David Novotny, Diane Larlus, and Andrea Vedaldi. Learning 3d object categories by looking around them. In *Proceedings of the IEEE International Conference on Computer Vision*, pages 5218–5227, 2017.
  - [30] Robert Osada, Thomas Funkhouser, Bernard Chazelle, and David Dobkin. Shape distributions. *ACM Transactions on Graphics (TOG)*, 21(4):807–832, 2002.
  - [31] Jeong Joon Park, Peter Florence, Julian Straub, Richard Newcombe, and Steven Lovegrove. DeepSDF: Learning continuous signed distance functions for shape representation. In *The IEEE Conference on Computer Vision and Pattern Recognition (CVPR)*, June 2019.
  - [32] Adam Paszke, Sam Gross, Soumith Chintala, Gregory Chanan, Edward Yang, Zachary DeVito, Zeming Lin, Alban Desmaison, Luca Antiga, and Adam Lerer. Automatic differentiation in pytorch. 2017.
  - [33] Charles R Qi, Hao Su, Kaichun Mo, and Leonidas J Guibas. Pointnet: Deep learning on point sets for 3d classification and segmentation. In *Proceedings of the IEEE Conference on Computer Vision and Pattern Recognition*, pages 652–660, 2017.
  - [34] Stephan R Richter and Stefan Roth. Matryoshka networks: Predicting 3d geometry via nested shape layers. In *Proceedings of the IEEE conference on computer vision and pattern recognition*, pages 1936–1944, 2018.
  - [35] Vincent Sitzmann, Julien Martel, Alexander Bergman, David Lindell, and Gordon Wetzstein. Implicit neural representations with periodic activation functions. *Advances in Neural Information Processing Systems*, 33, 2020.
  - [36] Miroslava Slavcheva, Maximilian Baust, Daniel Cremers, and Slobodan Ilic. Killingfusion: Non-rigid 3d reconstruction without correspondences. In *Proceedings of the IEEE Conference on Computer Vision and Pattern Recognition*, pages 1386–1395, 2017.
  - [37] Justin Solomon, Mirela Ben-Chen, Adrian Butscher, and Leonidas J. Guibas. As-killing-as-possible vector fields for planar deformation. *Comput. Graph. Forum*, 30(5), 2011.
  - [38] Olga Sorkine and Marc Alexa. As-rigid-as-possible surface modeling. In *Symposium on Geometry processing*, volume 4, pages 109–116, 2007.
  - [39] Jos Stam and Ryan Schmidt. On the velocity of an implicit surface. *ACM Transactions on Graphics (TOG)*, 30(3):1–7, 2011.
  - [40] Jian Sun, Maks Ovsjanikov, and Leonidas Guibas. A concise and provably informative multi-scale signature based on heat diffusion. In *Computer graphics forum*, volume 28, pages 1383–1392. Wiley Online Library, 2009.
  - [41] Michael Tao, Justin Solomon, and Adrian Butscher. Near-isometric level set tracking. In *Computer Graphics Forum*, volume 35, pages 65–77. Wiley Online Library, 2016.
  - [42] Maxim Tatarchenko, Alexey Dosovitskiy, and Thomas Brox. Multi-view 3d models from single images with a convolutional network. In *European Conference on Computer Vision*, pages 322–337. Springer, 2016.
  - [43] Maxim Tatarchenko, Alexey Dosovitskiy, and Thomas Brox. Octree generating networks: Efficient convolutional architectures for high-resolution 3d outputs. In *Proceedings of the IEEE International Conference on Computer Vision*, pages 2088–2096, 2017.
  - [44] Nanyang Wang, Yinda Zhang, Zhuwen Li, Yanwei Fu, Wei Liu, and Yu-Gang Jiang. Pixel2mesh: Generating 3d mesh models from single rgb images. In *Proceedings of the European Conference on Computer Vision (ECCV)*, pages 52–67, 2018.
  - [45] Weiye Wang, Duygu Ceylan, Radomir Mech, and Ulrich Neumann. 3dn: 3d deformation network. In *Proceedings of the IEEE Conference on Computer Vision and Pattern Recognition*, pages 1038–1046, 2019.
  - [46] Francis Williams, Jerome Parent-Levesque, Derek Nowrouzezahrai, Daniele Panozzo, Kwang Moo Yi, and Andrea Tagliasacchi. Voronoinet: General functional approximators with local support. In *Proceedings of the IEEE/CVF Conference on Computer Vision and Pattern Recognition Workshops*, pages 264–265, 2020.
  - [47] Francis Williams, Teseo Schneider, Claudio Silva, Denis Zorin, Joan Bruna, and Daniele Panozzo. Deep geometric prior for surface reconstruction. In *Proceedings of the IEEE Conference on Computer Vision and Pattern Recognition*, pages 10130–10139, 2019.
  - [48] Jiajun Wu, Chengkai Zhang, Tianfan Xue, Bill Freeman, and Josh Tenenbaum. Learning a probabilistic latent space of object shapes via 3d generative-adversarial modeling. In *Advances in neural information processing systems*, pages 82–90, 2016.
  - [49] Qiangeng Xu, Weiye Wang, Duygu Ceylan, Radomir Mech, and Ulrich Neumann. Disn: Deep implicit surface network for high-quality single-view 3d reconstruction. In *Advances in Neural Information Processing Systems*, pages 492–502, 2019.

## 7. Appendix

### 7.1. Additional Results

We provide a video file named `toy_figure.mp4` showing animation sequences of results and data used for the evaluation in Section 5.1. In addition, we provide video files `male.mp4` and `female.mp4`, showing animation sequences of learned interpolations from split 3 in the experiment described in Section 5.2. For splits 1 and 2, qualitative examples of interpolations between different humans are shown in Figure 11.

### 7.2. Ablation over $k$ , the number of affine fields

The main parameter of our method is  $k$ , the number of affine fields (see equation 7) in our multiple deformation prior loss. The intuition in setting  $k$  is that it should capture the number of different parts of a shape that move rigidly. To test the effect of  $k$  we designed the following experiment. We considered two input shapes  $\mathcal{X}_1, \mathcal{X}_2$  and trained using our loss as in equation 14, under different number values for  $k$ . In each run, all the other hyper-parameters were set to be the same:  $\lambda_e = 0.1$ ,  $\lambda_{ad} = 0.001$ ,  $\lambda_d = 0.001$  and  $D = 1$ . Figure 9 shows learned input reconstructions (far left and right); and in addition, it shows shapes generated by linear interpolation in the one dimensional latent space. Our findings can be summarized as follows: the number  $k$  serves merely as an upper bound to the number of deforming rigid parts that can be explained by the deformation prior loss. That is,  $k$  should not be set too small with respect to the expected number of independent deforming rigid parts, but other than that there is no harm in setting  $k$  to be much bigger. In figure 9 we see comparable results in quality for  $k \in \{5, 10, 15, 40, 200, 400\}$ . Note that setting  $k$  too small, as in  $k = 1$ , result in poor quality reconstructions. One question that might raise from these results is why should we limit the number of affine fields,  $k$ , at all? That is, setting  $k = |\mathcal{X}|$  by allowing a separate rigid deformation prior for each  $x \in \mathcal{X}$ . We see that for  $k = |\mathcal{X}|$ , we get high quality reconstruction as well. Nonetheless, deformations in latent space are no longer seem to be natural and fail to capture multiple parts rigid deformation between the two input shapes. This may be attributed to the fact that using a different, non-consistent affine field at every point allows too much flexibility and can reduce the killing loss without resulting in a near-rigid deformation.

### 7.3. Failure cases

Figure 8 shows some typical failures of our method. Left part depicts a test case from the removed punching sequence in split 2, whereas the right part is from the removed one leg jump sequence in split 1. In essence, although we demonstrate improvement over baselines there are still cases where the network fails to generalize to un-

seen poses. See the bend in the right arm in the left example and the missing parts from right hand in the right example. One possible solution could be to train our loss not only between pairs of latents in  $\mathcal{Z}$ , but also to more general latent samples in  $\mathbb{R}^D$  to allow better extrapolation.

### 7.4. Additional Implementation details

**Architecture.** Our architecture consists of two networks  $f : \mathbb{R}^3 \times \mathbb{R}^D \rightarrow \mathbb{R}$ , and the probability network  $\mathbf{p} = (p_1, \dots, p_k) : \mathbb{R}^3 \times \mathbb{R}^D \rightarrow \mathbb{R}^k$ . In all experiments in the paper we used  $D = 256, k = 20$ , unless stated otherwise. The network  $\mathbf{p}$  is implemented by a ReLU activation one-layer MLP with 128 hidden units. The network  $f$  is implemented by a 8-layers MLP, with a single skip connection between the input to the middle layer. There are 512 units in each hidden layer. Note that the same architecture was used in [31, 3, 18, 4]. For the initialization of  $f$  weights, we use the geometric initialization from [3]. We use the SoftPlus function, with  $\beta = 100$  for activation. The same architecture is used for the AutoDecoder baseline and for the decoder in the VAE baseline. For the encoder in the VAE baseline we use the same one as in [4].

Next, we describe additional details regarding the terms that consists our loss, see equation 14 in the main paper.

**Eikonal loss.** We utilize the Eikonal loss [18] to regularize the level-sets of implicit surfaces at intermediate latent codes  $\mathbf{z}_i$

$$\text{loss}_e(\theta) = \frac{1}{n} \sum_{i=1}^n (\|\nabla_{\mathbf{x}} f(\mathbf{y}_i, \mathbf{z}_i)\| - 1)^2, \quad (15)$$

where  $\mathbf{y}_i \in \mathbb{R}^3$  are sampled uniformly in a bounding box of all the input shapes.

**Deformation loss.** Here we give the missing details from the main text regarding the sampling of the points  $\mathbf{x}_i \in \mathcal{S}(\mathbf{z}_i)$ . We start by drawing a uniform sample of points  $\mathbf{p}_i$  in a bounding box of the shape  $\mathcal{S}(\mathbf{z}_i)$ . Then, we perform 5 iterations of the generalized Newton, defined by:

$$\mathbf{p}_i^{\text{next}} = \mathbf{p}_i - \frac{\nabla_{\mathbf{x}} f^T}{\|\nabla_{\mathbf{x}} f\|^2} f(\mathbf{p}_i). \quad (16)$$

Finally, we set  $\mathbf{x}_i = \mathbf{p}_i^{\text{next}} + \mathbf{n}_i$ , where  $\mathbf{n}_i$  is a random sample from a Gaussian noise  $\mathcal{N}(0, 0.02)$ .

**Reconstruction loss.** In order to approximate the input shapes  $\mathcal{X}^{(i)}$  at the latent codes  $\mathbf{z}^{(i)}$ , we use the SALD reconstruction loss [4] that handles raw data as input, and only requires the *unsigned* distance to the input geometry,



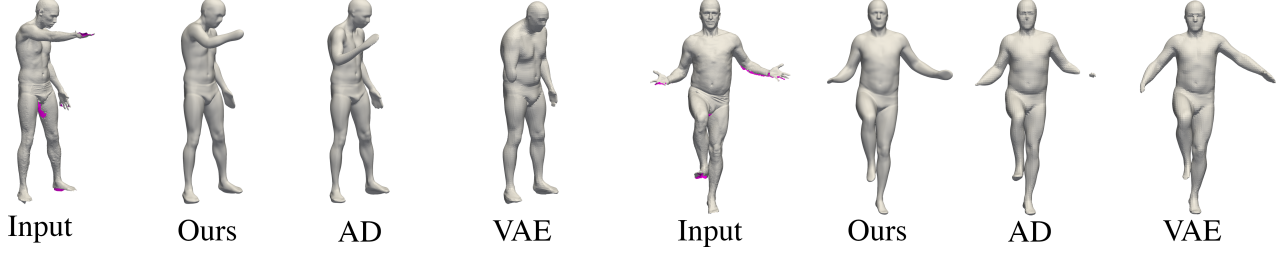


Figure 8: Failures in reconstructing unseen poses. From left to right (in each sequence of 4): unseen raw scan, ours, AD, VAE.

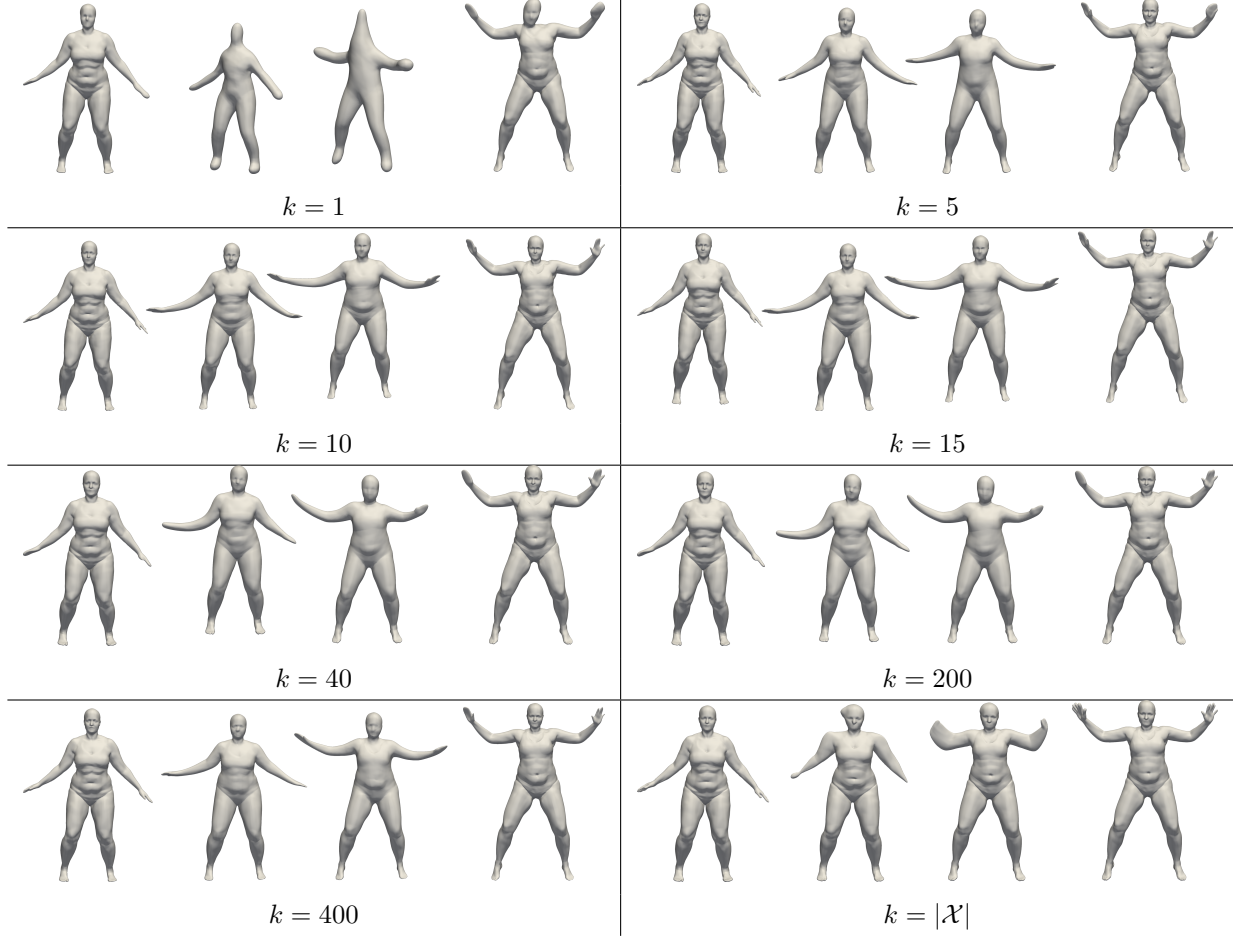


Figure 9: Ablation: experimenting with various  $k$  values, the number of affine fields. Left and right in each row are the learned reconstructions. The middle shapes were generated by latent interpolation.

$d(\mathbf{x}, \mathcal{X}) = \min_{\mathbf{y} \in \mathcal{X}} \|\mathbf{x} - \mathbf{y}\|$ . For a batch of size  $b$  of samples  $\mathbf{q}_i, \mathbf{z}^{(i)}, i \in [b]$ , the loss is defined by

$$\text{loss}_r(\theta) = \frac{1}{b} \sum_{i=1}^b \left[ \tau(f(\mathbf{q}_i, \mathbf{z}^{(i)}), d(\mathbf{q}_i, \mathcal{X}^{(i)})) + \lambda \tau(\nabla_{\mathbf{x}} f(\mathbf{q}_i, \mathbf{z}^{(i)}), \nabla_{\mathbf{x}} d(\mathbf{q}_i, \mathcal{X}^{(i)})) \right],$$

where  $\tau$  is the sign agnostic function, *i.e.*,  $\tau(a, b) = \min\{|a - b|, |a + b|\}$  for scalars, and  $\tau(\mathbf{a}, \mathbf{b}) = \min\{\|\mathbf{a} - \mathbf{b}\|, \|\mathbf{a} + \mathbf{b}\|\}$  for vectors. The latent  $\mathbf{z}^{(i)}$  is a random sample from  $\mathcal{Z}$ , and the point  $\mathbf{q}_i$  is sampled by adding random displacement  $\mathbf{n}_i$ , to a uniform sample from the input geometry  $\mathbf{x}_i \in \mathcal{X}^{(i)}$ . That is,  $\mathbf{q}_i = \mathbf{x}_i + \mathbf{n}_i$ . The displacement distribution is a mixture of two isotropic Gaussians,  $\mathcal{N}(0, \sigma_{i,1}^2 I)$  and  $\mathcal{N}_i(0, \sigma_{i,2}^2 I)$ .

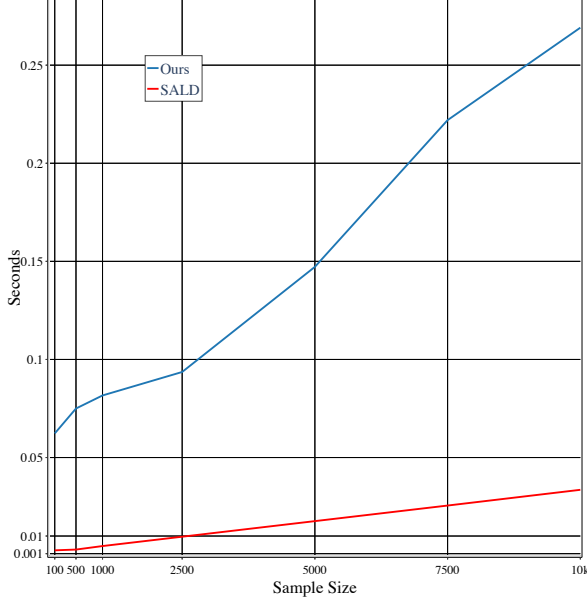


Figure 10: Timings. We report the time of a single forward pass (in seconds) as a function of sample size.

The parameter  $\sigma_{i,1}^2$  depends on each  $x_i$  and is set to be the distance of the 10<sup>th</sup> closest point to  $x_i$ , whereas  $\sigma_{i,2}$  was set to 0.3 fixed. Lastly, in all experiments we set  $\lambda = 0.1$ .

#### 7.4.1 Training details

In all the experiments in section 5.2, including baselines, training was done using the ADAM [22] optimizer, with batch size  $b = 64$ . For the VAE, we set a fixed learning rate of 0.0005. The same learning rate was set for the AD, except for the learning rate of the latents  $\{z^{(i)}\}$ , which was set to 0.001. For splits 1 and 2, networks were trained for 5000 epochs. The loss parameter  $\lambda_d$  was set according to the following scheduling:  $\lambda_d = 0$  for the first 2000 epochs, followed by  $\lambda_d = 0.001$  for the next 2000 epochs, and  $\lambda_d = 0.0001$  for the last 1000 epochs. For splits 3 and 4, training was done for 50k epochs. The scheduling for  $\lambda_d$  was to set  $\lambda_d = 0$  for the first 20k epochs, followed by  $\lambda_d = 0.001$  for the next 20k epochs, and  $\lambda_d = 0.0001$  for the last 10k epochs. Training was done on 4 Nvidia V-100 GPUs, using PYTORCH deep learning framework [32]. For the evaluation in section 5.1, training was for 5000 epochs for all experiments, on a single Nvidia V-100 GPU. The batch size was  $b = 8$ . In addition, we set  $\lambda_d = 0.001$  fixed.

**Timings.** In figure 10 we report the total seconds required for a single forward pass, on a single Nvidia V-100 GPU. The baseline for comparison is SALD [4]. In the experiments in Section 5.2, a sample size of 2500 points was used, resulted in approximately 9.7 times slower training

than SALD. The main additional cost in our method can be attributed to the calculation of the network’s second derivatives, as part of the calculation of the rigid deformation prior.

#### 7.4.2 Evaluation metrics

We used two different metrics to measure distances between shapes. One metric is the *Chamfer* distance,  $d_C$ , measuring the squared distance between each point in one shape to its nearest neighbour in the other. Second metric is the *Wasserstein* distance,  $d_W$ , which measures the sum of the distances of the optimal transportation between the shapes. See [1] for more details about these two metrics. Next, we present the formal definition for these metrics. The definition of the *Chamfer* distance is

$$d_C(\mathcal{X}_1, \mathcal{X}_2) = \frac{1}{2} (d_C^{\rightarrow}(\mathcal{X}_1, \mathcal{X}_2) + d_C^{\rightarrow}(\mathcal{X}_2, \mathcal{X}_1)) \quad (17)$$

where

$$d_C^{\rightarrow}(\mathcal{X}_1, \mathcal{X}_2) = \frac{1}{|\mathcal{X}_1|} \sum_{x_1 \in \mathcal{X}_1} \min_{x_2 \in \mathcal{X}_2} \|x_1 - x_2\|^2. \quad (18)$$

The definition for the *Wasserstein* distance is

$$d_W(\mathcal{X}_1, \mathcal{X}_2) = \min_{\phi: \mathcal{X}_1 \rightarrow \mathcal{X}_2} \sum_{x \in \mathcal{X}_1} \|\phi(x) - x\| \quad (19)$$

where  $\phi$  is a bijection. Note that  $d_W$  inputs of equal size. In tables 1 and 2 we evaluated  $d_C$  on samples of size 30k points, and  $d_W$  on samples of size 1k points.

#### 7.4.3 Danskin’s Theorem

**Theorem 1** (Danskin). *Let  $g : \mathbb{R} \times \Omega \rightarrow \mathbb{R}$  be a continuous function, continuously differentiable in its first argument, where  $\Omega \subset \mathbb{R}^d$  is a compact set. Let*

$$G(t, \mathbf{x}) = \min_{\mathbf{x} \in \Omega} g(t, \mathbf{x}). \quad (20)$$

Then

$$\frac{\partial G}{\partial t}(t, \mathbf{x}) = \frac{\partial G}{\partial t}(t, \mathbf{x}_*),$$

when  $\mathbf{x}_*$  is the unique minimizer of eq. (20).

This version of Danskin’s Theorem follows directly from Corollary 10.1 in [5].



Figure 11: Interpolation of latent codes between different humans. Each block of three rows shows (top to bottom): Our result, AD, and VAE.